CrossMark

REGULAR PAPER

Shaofei Wang · Yujia Chen · Ying Zheng Liu

Measurement of unsteady flow structures in a low-speed wind tunnel using continuous wave laser-based TR-PIV: near wake behind a circular cylinder

Abstract The unsteady measurement of spatiotemporally varying flow structures in a low-speed wind tunnel using a continuous wave (CW) laser-based time-resolved particle image velocimetry (TR-PIV) setup was extensively evaluated in the near wake behind a circular cylinder. A CW laser with a maximum power of 25 W in combination with a high-speed camera operating at 7 kHz was used to determine the wake flows at two different free-stream flow speeds: $U_0 = 5$ and 10 m/s. Three different camera exposure times were selected for comparison: $\tau = 20$, 50, and 80 μs. In the experiments, the low-repetition conventional PIV setup using the high-power pulsed laser ($\tau = 8$ ns, 135 mJ/pulse) was used to determine the time-mean and statistical flow quantities, which served as the reference for determining the deviation in the TR-PIV measurements. At the lower flow speed of $U_0 = 5$ m/s, the time-mean-separated flow patterns and the streamwise velocity profiles in all of the TR-PIV systems showed satisfactory agreement with the conventional PIV measurements, along with accurate capture of the large-scale Karman vortex and its harmonic behaviors. At the higher flow speed of $U_0 = 10$ m/s, the measurement at $\tau = 50$ μs gave a relatively accurate representation of the statistical flow quantities. At the longest exposure time of $\tau = 80$ μs, considerable deviations in the time-mean streamwise fluctuation intensity and the TKE (turbulence kinetic energy) were observed due to the streaky particle image. The strong swirling motion of the large-scale vortical structures increased the deviation in the TR-PIV measurements, which increased with the increasing camera exposure time. Further POD analysis demonstrated that the leading energetic modes in the system with $\tau = 50$ μs accurately determined the spatial features of the Karman-like vortex and its harmonic events. However, inaccurate vector representation of the second harmonic events was observed in the system with $\tau = 80$ μs. Finally, for both flow speeds, the lower-order reconstructed phase-dependent representations of the Karman-like vortex and its harmonic behaviors were composed of the time-series velocity vector fields determined using the system with $\tau = 50$ μs, thus providing a straightforward quantitative view of the coupled unsteady events.

Keywords Unsteady measurement · TR-PIV · Exposure time · CW laser · Flow structure

List of symbols
D Diameter (m)
Re Reynolds number
u Instantaneous streamwise velocity (m/s)
U_0 Free-stream velocity (m/s)

S. Wang · Y. Chen · Y. Z. Liu (✉)
Key Lab of the Education Ministry for Power Machinery and Engineering, School of Mechanical Engineering, Shanghai Jiao Tong University, 800 Dongchuan Road, Shanghai 200240, China
E-mail: yzliu@sjtu.edu.cn

S. Wang · Y. Chen · Y. Z. Liu
Gas Turbine Research Institute, Shanghai Jiao Tong University, 800 Dongchuan Road, Shanghai 200240, China

$\overline{u}$	Time-averaged streamwise velocity (m/s)
u'	Fluctuating portion of the streamwise velocity (m/s)
u'_{rms}	Root-mean square of the streamwise velocity fluctuations (m/s)
x	Streamwise coordinate (m)
y	Longitudinal coordinate (m)
St	Strouhal number
$a(t)$	POD mode coefficient
n	Eigenmode number

Greek symbols

τ	Exposure time (s)
λ_n	POD eigenvalue
ϕ	POD eigenfunction

Abbreviations

CMOS	Complementary metal oxide semiconductor
CW	Continuous wave
PIV	Particle image velocimetry
POD	Proper orthogonal decomposition
TKE	Turbulence kinetic energy
TR-PIV	Time-resolved particle image velocimetry

1 Introduction

The recent developments in state-of-the-art hardware (e.g., cameras and lasers) and image-processing algorithms have stimulated considerable improvements in particle image velocimetry (PIV). The conventional PIV setup ("conventional PIV" hereafter), which typically comprises a low-repetition pulsed laser (around 15 Hz) and a CCD camera, enables accurate determination of the time-mean and statistical flow quantities. However, the sampling frequency of this configuration generally lags far behind the demand for unsteady measurements, particularly in low-speed wind tunnel tests. The time-resolved PIV (TR-PIV) approach, which uses a high-speed camera in combination with a high-repetition pulsed laser, can provide access to spatiotemporally varying flow fields at sampling rates of the order of kHz or ever higher (Beresh et al. 2015; Coletti et al. 2013; Sampath and Chakravarthy 2014). Nonetheless, the high-cost and maintenance requirements of the high-repetition high-power pulsed lasers are a practical barrier to the widespread use of time-accurate TR-PIV measurements in wind tunnels. However, the high-power continuous wave (CW) laser can serve as a cost-effective alternative (Elzawawy 2012; Willert 2015) in low-speed air flow measurements.

The literature shows that a CW laser fitted with a high-speed camera can successfully measure the unsteady flows in low-speed water channels (Hout 2011; Shi et al. 2010; Shinohara et al. 2004; Wang and Liu 2016), with a moderate power output laser providing adequate illumination. However, when targeted for measuring the air flow in a low-speed wind tunnel, this configuration is challenged by the weak light scattered by the relatively fine particles and the streaky particle images resulting from the long exposure times (10^1–10^2 μs) (Elzawawy 2012; Willert 2015). Using an Argon ion continuous laser with maximum power of 5 W, Elzawawy (2012) measured the canonical turbulent boundary layer flows at two different free-stream speeds: $U_0 = 5.5$ and 11 m/s. The seeded air fluid flow in the field-of-view region of 70 mm × 30 mm was imaged by a high-speed camera operating at 5 kHz with three different exposure times, i.e., $\tau = 50$, 100, and 150 μs. Using the conventional PIV measurements with a high-power pulsed laser as the baseline configuration, the TR-PIV results showed favorable agreement of the time-mean velocity profiles at $U_0 = 5.5$ m/s for all exposure times. However, the high-order quantities, such as the velocity fluctuation intensity and Reynolds stress, exhibited considerable deviation, showing discrepancies of over 100%. The deviation was attributed to the streaky particle images stemming from the long exposure time. Moreover, increasing the flow speed to $U_0 = 11$ m/s gave rise to substantial deviation in the flow quantities. A similar evaluation was recently performed by Willert (2015) using a high-speed camera and a 6-W CW laser, which was targeted for the efficient sampling of turbulence quantities. The boundary layer flow in a low-speed wind tunnel was measured at a sampling frequency of over 10 kHz. Because the free stream speed was kept at 4 m/s, an exposure time of $\tau = 20$ μs was specifically chosen for the camera to reduce the streaking of the particle images on the camera sensor. Given that the short exposure time and high framing rate significantly reduced the amount of light projected on the camera sensor, the light sheet

was limited to a very narrow strip with a width of 4–8 mm. The time-mean velocity profiles showed favorable agreement with the corresponding profiles using the conventional PIV and the data determined from the direct numerical simulation. However, considerable mismatches in the root-mean-squared streamwise velocities and the log-law indicator functions were readily apparent, reading over 50% discrepancy in particular regions. Limited by the extremely narrow measurement region, not much information of flow structure was identified by this technique. The abovementioned studies sought to determine the statistical flow quantities using TR-PIV measurements. However, no study has examined the feasibility of using CW laser-based TR-PIV to determine the dynamics of the spatiotemporally varying flow structures buried in turbulent flows, even though this setup has important advantages over the conventional PIV approach and pointwise measurement techniques such as hotwire.

The focus of this study was to assess the unsteady measurement of the flow structures in a low-speed wind tunnel using a CW laser-based TR-PIV setup. To achieve this, the near wake behind the circular cylinder was used as the benchmark configuration. A CW laser with the maximum power of 25 W in combination with a high-speed camera operating at 7 kHz was used to determine the wake flows at two different free-stream flow speeds, i.e., $U_0 = 5$ and 10 m/s. According to previous studies (Elzawawy 2012; Willert 2015), the considerable increase in laser power should ensure time-accurate variation in the highly unsteady flow at the tailored exposure time of the camera. Three different exposure times for the high-speed camera were selected for comparison: $\tau = 20$, 50, and 80 µs. In the experiments, a low-repetition PIV setup using a high-power pulsed laser ($\tau = 8$ ns, 135 mJ/pulse) was used as the baseline configuration, which provided a database of the time-mean and statistical quantities for determining the deviation in the TR-PIV measurements. Finally, the unsteady events buried in the near wake were delineated using proper orthogonal decomposition (POD) analysis.

2 Experimental apparatus

The experiments were performed in a subsonic open-circuit wind tunnel previously used by Liu et al. (2011) and Zhang and Liu (2012). A honeycomb and five screens were placed in sequence in the settling chamber. A diffuser and a smooth contraction fairing with a contraction ratio of 6:1 were used to straighten the flow. The dimensions of the inlet channel were 300 mm (width) × 300 mm (height) × 1000 mm (length). Air was driven by a centrifugal blower using a 1.5-kW motor. The test section was 300×300 mm^2 in cross section and 2000 mm in length. The speed of the flow in the test section was controlled using an inverter (Danfoss, Denmark). As shown in Fig. 1a, a circular cylinder spanning the entire width was placed in the middle of the test channel. The two-dimensional circular cylinder was 30 mm in diameter, and the blockage ratio of the cylinder was 10%. The free-stream turbulence intensity measured by a single-wire probe (55P11, Dantec Inc., Denmark) was less than 0.6% at flow speeds of 5–25 m/s. To evaluate the performance of the TR-PIV system, the flows were tested at the free-stream wind speeds of 5 and 10 m/s, which, based on the cylinder diameter, correspond to the Reynolds numbers $Re = 1.0 \times 10^4$ and 2.0×10^4, respectively. The
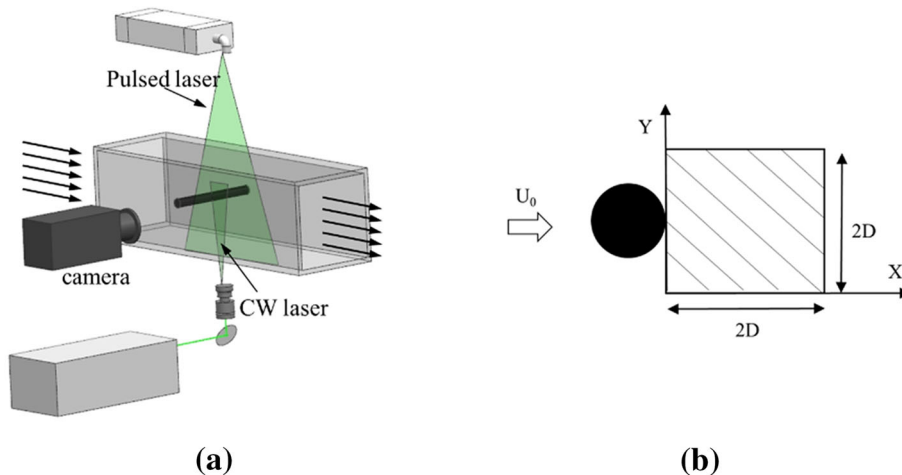

Fig. 1 Schematic diagram of the PIV measurement setup (**a**) and coordinate system (**b**)

global seeding of the complete wind tunnel volume was conducted using di-ethyl-hexyl-sebacat (DEHS) droplets generated by an aerosol atomizer (PIVPart14, PIVTEC-GmbH, Germany), leading to a polydisperse distribution with a mean diameter of approximately 1 μm. To ensure stable and homogeneous distributions of the seeding particles across all of the PIV measurements, the wind tunnel facility was entirely covered in a closed tunnel made of Plexiglas, creating closed-loop circulation of the seeded air flow (Wang et al. 2014). A large number of DEHS droplets were added to the closed tunnel, and the air was circulated for a couple of minutes to create high-quality seeding patterns in the PIV images.

A TR-PIV system comprising a high-speed complementary metal oxide semiconductor (CMOS) camera (PCO, USA) and a high-power 25-W CW laser (Spectra physics, USA) was used to determine the highly unsteady wake flow behind the circular cylinder. An appropriate combination of cylindrical lenses was fitted to the compact laser to produce a 1 mm thick light sheet around the cylinder. To improve the quality of the particle images, the illumination was limited to the $2D \times 2D$ region immediately behind the cylinder (Fig. 1b). The CMOS camera was operated at a resolution of 1000×1000 pixels and a framing rate of 7000 Hz, which was sufficient to cover the range of frequencies of interest. The measurements using the TR-PIV system were tested at three different exposure times, i.e., $\tau = 20, 50,$ and 80 μs. A total of 30,001 images of the seeded flow were successively acquired in each run of measurements, and every two neighboring images were cross correlated, resulting in 30,000 instantaneously varying velocity vector maps. The time-mean and statistical velocity quantities measured using the conventional PIV setup were used as the reference for comparison with the TR-PIV measurements. An Nd:YAG laser with 135 mJ/pulse (532 nm, 8 ns, Litron, UK) was used to illuminate the particle image in the near wake region of the cylinder. The CMOS camera operated at 1 Hz in double-frame mode and sampled 6000 instantaneously varying vector maps, which was more than enough to ensure the statistical convergence of the velocity field for comparison. A multigrid cross-correlation technique was used to post-process the particle images captured by the TR-PIV system and the conventional PIV system, with a final interrogation window size of 32×32 pixels. A 50% overlap of the interrogation windows in both the horizontal and vertical directions was applied, which yielded a measurement grid of the velocity vectors with a spacing of 1.3 mm $\times$ 1.3 mm. The error in measuring the particle displacement between two images was less than 0.1 pixels, and the uncertainty levels for the measured velocity components were estimated to be within $\pm 2\%$ of the actual values_ENREF_3_ENREF_3.

3 Results and discussion

As mentioned above, TR-PIV measurements are subject to the possible problem of streaky particle images. Thus, a straightforward view of this issue can be gained by plotting a particle image at different exposure times at two different free stream speeds (Fig. 2). The particle image corresponding to the conventional PIV using a pulsed laser is also supplied as a reference. When the pulsed laser is used, the particle density in the captured image is satisfactory at the two flow speeds. The particles remain circle dot patterns, thus providing well-captured images for cross correlation with the resultant accurate determination of the velocity vector
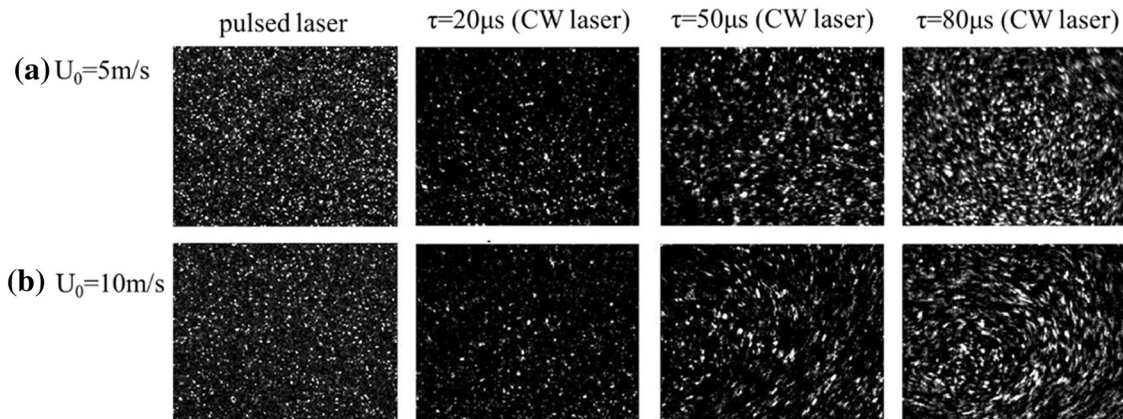

Fig. 2 Particles' images from the PIV measurements with different exposure times

field. When the CW laser is used and the CMOS camera is operated with an exposure time of $\tau = 20$ µs, the number of particles in the image is considerably reduced, while the particles' shape does not show an obvious streaky pattern. A slight reduction in the particle density is observed as the flow speed increases from 5 to 10 m/s. Increasing the exposure time to $\tau = 50$ µs results in increases in the particle density and particle size, which can be attributed to the increased exposure of the particles to the illumination. Thus, close examination of the particle image ($\tau = 50$ µs) at 5 m/s shows a slightly streaky particle shape, whereas at the higher flow speed of 10 m/s the streaky particle pattern is readily recognizable. When the exposure time is increased to 80 µs, a substantial increase in the particle density is observed, while the streaky particle shapes even overlap at 5 m/s. This issue is more pronounced at the higher flow speed of 10 m/s, with the prominent streaky particle pattern also reflecting the swirling motion of the vortex structures. Accordingly, the effect of the exposure time on the time-mean and statistical velocity fields needs to be quantified, and separate assessments and analyses are provided for the two different flow speeds in the subsequent sections.

3.1 Wake flow at $U_0 = 5$ m/s

Figure 3 shows a comparative view of the time-mean vector patterns ($U_0 = 5$ m/s) in the four different measurement conditions, i.e., the conventional PIV measurement using a pulsed laser and the TR-PIV measurements at $\tau = 20$, 50, and 80 µs, and the contour of the streamwise velocity component is superimposed to assist the interpretation of the flow patterns. A global view of the figures shows a similar pattern in the near wake region, which features a pair of low-speed clockwise and counterclockwise recirculation zones. The length of the recirculation zone, which is estimated from the trailing edge of the circular cylinder to the saddle point in the vector pattern, is $1.4D$ for all systems. The streamwise velocity contours demonstrate globally similar patterns in all of the systems.

The influence of the exposure time on the flow field is quantitatively assessed by plotting the profiles of the time-mean streamwise velocity, the streamwise velocity fluctuation intensity, and the turbulence kinetic energy (TKE) along the various streamwise stations ($x/D = 0.4$–1.2) in Fig. 4. Consistent with Fig. 3, the time-mean streamwise velocity profiles corresponding to the three different exposure times (Fig. 4a) show favorable agreement with the measurements using the pulsed laser, although closer examination reveals slight discrepancies along the upper and lower shear layers. At station $x/D = 0.4$, no appreciable motion of the fluid can be discerned in the bulk area of the low-speed recirculation zone ($y/D = -0.5$ to 0.5). Beyond that zone in the longitudinal direction, the streamwise velocity component sharply increases to $u/U_0 = 1.2$
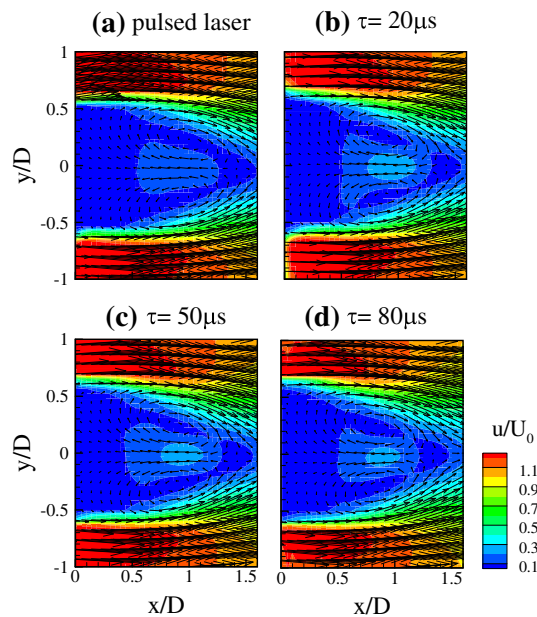

Fig. 3 Vector patterns and contour plot of the time-averaged streamwise velocity ($U_0 = 5$ m/s): pulsed laser (**a**), CW laser with an exposure time of 20 µs (**b**), 50 µs (**c**), and 80 µs (**d**)
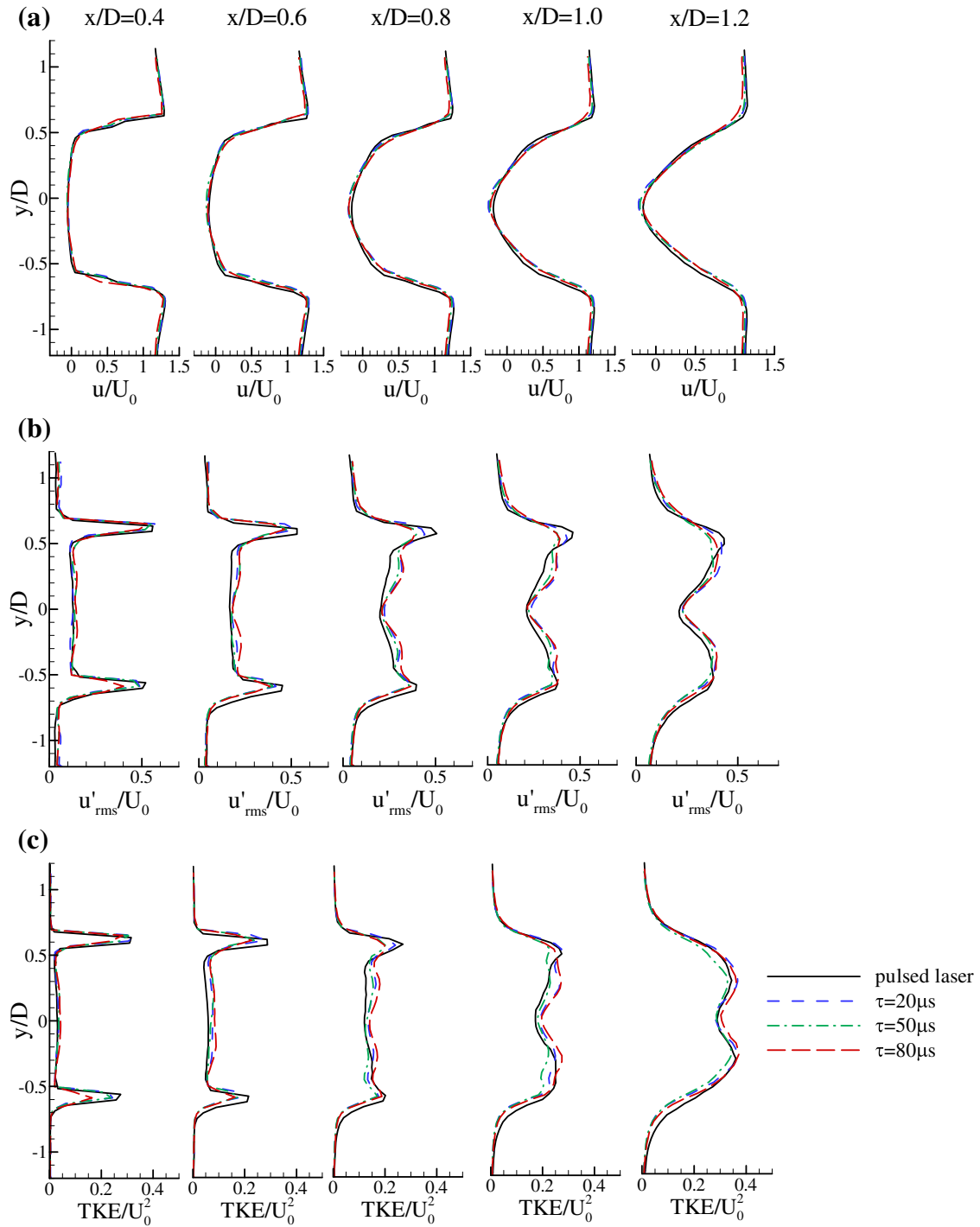
Fig. 4 Profiles of time-averaged streamwise velocity (**a**), time-averaged streamwise velocity fluctuation intensity (**b**), and turbulence kinetic energy (**c**) along $x/D = 0.4$–1.2 ($U_0 = 5$ m/s)

at $y/D = \pm 0.7$, and then slowly reduces to $u/U_0 = 1.1$. As the fluid flows downstream, the longitudinal size of the recirculation zone is reduced, along with apparently reversed flow. Beyond station $x/D = 0.8$, the reversed velocity magnitude in the center of the recirculation zones is slightly underestimated by the measurements using the TR-PIV system. With the increasing exposure time, the reversed flow speed in the central recirculation zone is close to that in the conventional PIV. When the longest exposure time

$\tau = 80$ µs is used, the discrepancy is observed in the high-speed region beyond $y/D = \pm 0.6$, particularly near the upper and lower separated shear layers featured by the sharp velocity gradient and the superimposed energetic vortical structures. This error can again be attributed to the streaky particles associated with the high-speed and swirling motions.

Figure 4b shows the profiles of the time-mean streamwise velocity fluctuation intensities. At station $x/D = 0.4$, the conventional PIV measurement using the pulsed laser identifies a pair of strips with peak fluctuation intensities of around 0.5 in the narrow region of $y/D = \pm(0.5–0.7)$, which are signatures of the convective vortices superimposed in the upper and lower separated shear layers, whereas the fluctuation intensity in the recirculation zone is low at 0.15. For the TR-PIV measurements with exposure times of 20 and 50 µs, the fluctuation intensities agree well with those determined by the conventional PIV. However, increasing the exposure time to 80 µs results in a substantial reduction in the peak fluctuation intensity. At the downstream stations, the measurements using the pulsed laser show a progressive reduction in the peak intensity magnitude along with a distinct expansion of the large fluctuation intensity plateau along the longitudinal direction, as a result of the pairing processes of the growing vortices. At station $x/D = 1.2$, the peak fluctuation intensity is reduced to 0.4 in the separated shear layers, and increases to 0.2 in the central recirculation zone. Close examination of the profiles in the region of $x/D = 0.6–1.2$ reveals that the fluctuation intensities determined by the TR-PIV systems are generally overestimated in the recirculation zone ($-0.4 < y/D < 0.4$), but underestimated in the upper and lower separated shear layers. Of the three exposure times, the profile corresponding to the moderate exposure time of $\tau = 50$ µs shows the most satisfactory agreement with the profile determined by the pulsed laser in the central recirculation zone.

Figure 4c shows the profiles of the TKE. At station $x/D = 0.4$, the measurement using the pulsed laser identifies the occurrence of the peak TKE = 0.3 in the upper and shear layers ($y/D = \pm(0.5–0.7)$), while the TKE in the central recirculation zone is kept at the minimum state. Along with the development of the superimposed vortices, the TKE is effectively intensified in the bulk region of the wake, particularly in the recirculation zone. At station $x/D = 1.2$, the peak TKE reaches 0.4 at $y/D = \pm 0.3$. Compared with the streamwise velocity fluctuation intensity, the measurements using the TR-PIV system with different exposure times demonstrate a smaller discrepancy from the measurements using the pulsed laser, but are still slightly overestimated in the central recirculation zone. The profiles corresponding to the exposure time of 50 µs show generally good agreement at the five streamwise stations.

The above discussion indicates that there are appreciable discrepancies in the high-order flow quantities due to the streaky particle image, which results in spatially selective underestimation and overestimation in the separated shear layers and the central recirculation zones, respectively. Further comparison is made of the longitudinal velocity spectra at $x/D = 1$ and $y/D = 0.5$ extracted from the TR-PIV measurements with different exposure times (Fig. 5). Because the measurements using the pulsed laser were made at a very low sampling rate, no reference data are supplied here for comparison. As shown in Fig. 5, a dominant peak is observed at $St = 0.21$ for all of the TR-PIV measurements, which is assigned to the large-scale Karman-like vortices buried in the wake. The peak at $St = 0.42$ is identified as the second harmonic frequency, whereas
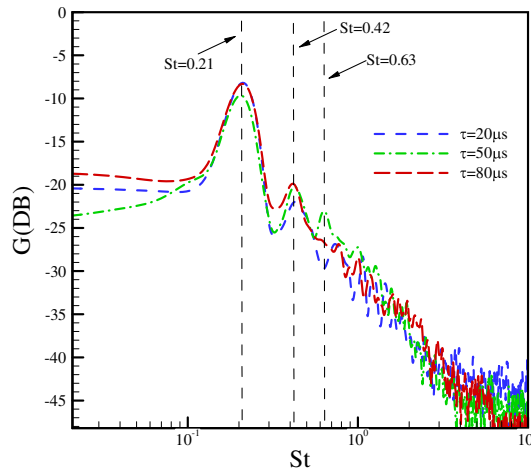

Fig. 5 Streamwise velocity spectra at location ($x/D = 1$, $y/D = 0.5$) ($U_0 = 5$ m/s)

the third harmonic event at $St = 0.63$ is only discerned at $\tau = 50$ μs, and the measurements at the other two exposure times fail to capture this event.

To examine the influence of the exposure time on the spatial characteristics of the energetic flow structures that dominate the unsteady behavior of the wake, we perform a snapshot POD (Sirovich 1987) of the four datasets. POD is a mathematical technique for extracting a basis for the modal decomposition of an ensemble of signals (Kim et al. 2005). Simultaneous acquisition of the sequential velocity data at a large number of spatial points using the PIV provides an attractive basis for POD (Kim et al. 2005). Prior to showing the decomposed flow pattern of the cylinder wake, the POD method used in the study is first briefly introduced. The general goal of POD is to find the optimal representation of the field realizations, which lead to a Fredholm integral equation of the so-called classical POD,

$$\int R(x, x')\phi(x')\mathrm{d}x' = \lambda\phi(x). \tag{1}$$

Here, $R(x, x')$ is the two-point correlation matrix of the realizations of the random field,

$$R(x, x') = \langle u(x)u^*(x') \rangle. \tag{2}$$

The operator $\langle \cdots \rangle$ and the asterisk denote the ensemble average and complex conjugate, respectively, and $u(x)$ is the instantaneous flow field. The eigenvalue λ_n of Eq. (1) has a finite set of eigenfunctions: $\phi_n(x)(n = 1, \ldots, N)$ (N is the number of grid points of each flow realization), which represent certain modes in the flow field. The eigenfunctions are sometimes referred to as coherent structures because the structures are highly correlated in an average sense within the flow field (Gurka et al. 2006).

Figure 6 depicts the eigenvalues of the first 10 POD modes of the velocity fields, which represent the relative contributions of the eigenmodes to the total fluctuation energy. A global view of Fig. 6 reveals a favorable match of all of the measurements in the variations of the eigenvalues, such that as the mode number increases, the eigenvalues decrease rapidly and approach zero. For the conventional PIV measurement using the pulsed laser, the contributions of the first two modes to the total fluctuation are 37.2 and 19.3%, respectively, whereas the contributions of the third and fourth modes are 6 and 3%, respectively. As discussed later in this section (Fig. 7), the first and second pairs of modes represent the Karman-like vortex and its second harmonic event, respectively. However, for the TR-PIV system, the eigenvalues of the first two modes are slightly larger, and increase with the increasing exposure time, reaching 37.8 and 20.5% at $\tau = 20$ μs, 38.5 and 21.9% at $\tau = 50$ μs, and 41.9 and 23.0% at $\tau = 80$ μs, respectively. This trend arises because the small-scale vortices or high-frequency fluctuations buried in the near wake are submerged by the streaky particle image, which results in the relatively larger contributions of the large-scale vortical structures in each dataset.

The influence of the exposure time on the spatial characteristics of the energetic flow structures in the near wake is determined by plotting the leading eigenmodes. Figure 7 shows the eigenmodes of the first four POD modes determined by all of the systems, in which the contours of the longitudinal component are superimposed in the vector pattern to facilitate interpretation of the flow structures. The spatial patterns of
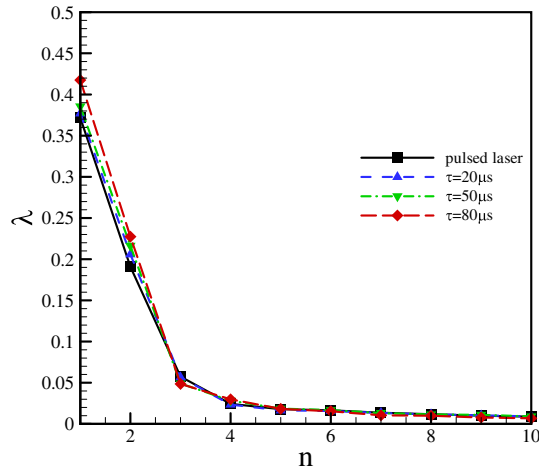

Fig. 6 Eigenvalues of the first 10 POD modes of the velocity fields measured with different exposure times ($U_0 = 5$ m/s)
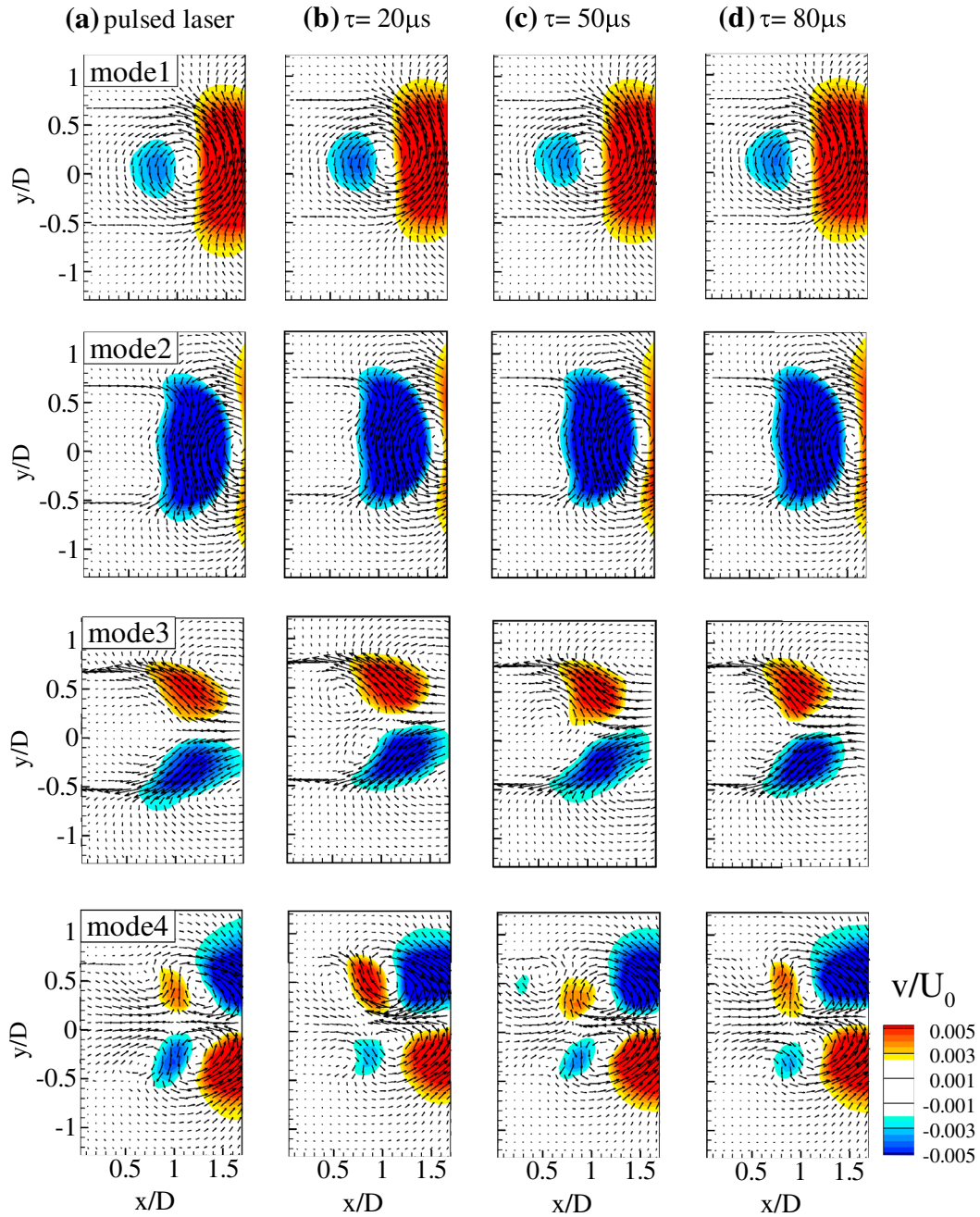
Fig. 7 Spatial patterns of the first four POD modes (U_0 = 5 m/s): pulsed laser (**a**), CW laser with an exposure time of 20 μs (**b**), 50 μs (**c**), and 80 μs (**d**)

the first two POD modes corresponding to the measurement using the pulsed laser mainly feature the Karman vortex street. The two paired modes exhibit a streamwise shift of the large-scale vortical structure, which, together with the corresponding time-varying mode coefficients, reflect the convective motion of the structure. In the first mode, a counterclockwise large-scale vortical structure is located at $x/D = 1.1$, whereas, in the second mode, a counterclockwise large-scale vortical structure is centered at $x/D = 1.6$. The vector patterns for the TR-PIV measurements with the three different exposure times (Fig. 7b–d) demonstrate perfect similarity in spatial variation. The spatial patterns of the third and fourth POD modes mainly feature the harmonic representation of the Karman-like vortex. Compared with the first pair of POD modes, the difference between the measurements using the pulsed laser and the continuous laser in the second pair

is noticeably greater. The third eigenmode clearly shows the existence of two small structures slightly asymmetrically distributed near the station $x/D = 0.7$ at $\tau = 20$ μs (Fig. 7b). However, this is not the case for the counterparts in the three TR-PIV systems. In the fourth eigenmode of the measurements using the pulsed laser, two pairs of symmetrically distributed structures are located at the stations $x/D = 0.7$ and 1.3. Although similar structures in the fourth eigenmode can be observed in the counterparts of the three TR-PIV systems, close examination of the complex pattern near the station $x/D = 0.9$ indicates that there is relatively good similarity between the structure measured by the pulsed laser and the one at $\tau = 50$ μs (Fig. 7c).

Figure 8 shows the spectra of the first and third POD mode coefficients of the realizations determined by the three TR-PIV systems. Similar spectral features can be observed with the second and fourth POD mode coefficients, which are not supplied here for clarity. For the first mode in all three systems (Fig. 8a), the peak events with close spectrum magnitude can be readily identified at $St = 0.21$, and the spectrum plateaus centered at $St = 0.21$ are also well matched. This, along with the discussion in Fig. 7, indicates that the exposure times of 20–80 μs used in the TR-PIV measurements do not exert an appreciable influence on the spatial and spectral (or temporal) characteristics of the overwhelmingly dominant Karman vortex street. It is notable that compared with the spectrum of the velocity fluctuations at a discrete position in the flow field (Fig. 5), the spectrum of a POD mode coefficient characterizing the dominant flow structure would give a relatively accurate representation of the temporal/spectral senses because the single point velocity information is usually subjected to the background noise. Figure 8b depicts the spectra of the third POD mode coefficients, in which the peak frequency at $St = 0.42$ can be readily recognized and the spectrum centered at $St = 0.42$ exhibits a more appreciable difference for the three systems with different exposure times.

The foregoing discussion reveals that the time-mean and statistical quantities of the flow fields determined by the TR-PIV setup with the three different exposure times all moderately agree with those determined by the conventional PIV setup using the pulsed laser. A similar level of agreement is also established for the spatial patterns of the leading energetic POD eigenmodes. This means that the streaky particle images observed at the different exposure times (20–80 μs) (Fig. 2a) do not incur the appreciable discrepancies of the captured dominant unsteady behavior. Hereafter, the dataset for the exposure time of
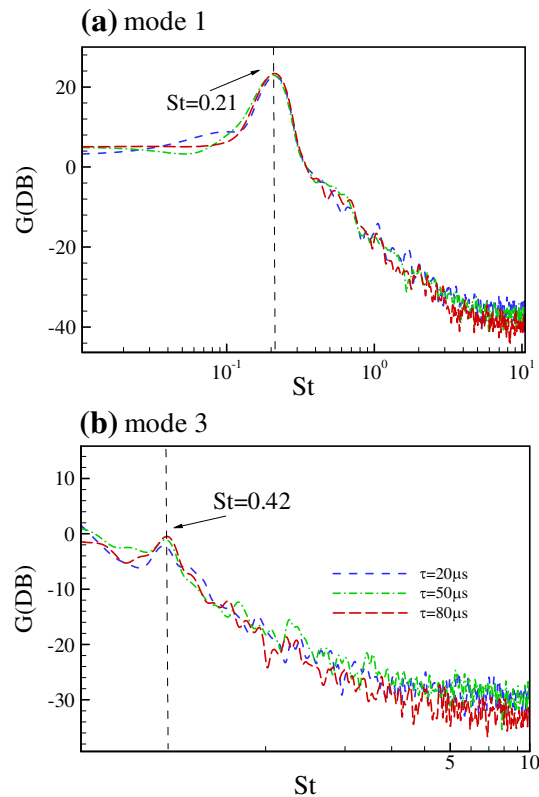

Fig. 8 Spectra of the first and third POD mode coefficients ($U_0 = 5$ m/s)

$\tau = 50$ μs is used to delineate the phase-averaged unsteady events buried in the near wake region. According to Van Oudheusden et al. (2005), the POD coefficients of the first pair of POD modes, i.e., $a_1(t)$ and $a_2(t)$, serve as an accurate phase signal for phase averaging the flow fields, which enables us to explore the phase-dependent patterns of the large-scale events buried in the wake. These two coefficients are correlated in the following circular manner,

$$r^2 = \frac{a_1(t)^2}{2\lambda_1} + \frac{a_2(t)^2}{2\lambda_2}. \tag{3}$$

Accordingly, a circular correlation between $a_1(t)/\sqrt{2\lambda_1}$ and $a_2(t)/\sqrt{2\lambda_2}$ is established, from which the phase information of the time-dependent low-order flow model can be determined. The correlation map of the first two POD mode coefficients is plotted in Fig. 9. The circular distribution of the correlation coefficients shown in Fig. 9 indicates the cycle-to-cycle variations in the Karman-like vortex shedding process, whereas the scattered radial magnitude reflects the strength of each vortex shedding process (Wang et al. 2014).

From the correlation map of the first paired POD mode coefficients in Fig. 9, it is possible to determine the phases of the corresponding instantaneous flow fields. In the phase-averaging calculation, a total of eight phases of the Karman-like vortex shedding process are determined at a phase interval of 45°. Two separate reconstruction processes are first performed using the first (modes 1 and 2) and second (modes 3 and 4) pairs of POD modes, which represent the Karman-like vortex shedding process at $St = 0.21$ and its harmonic event at $St = 0.42$, respectively. Here, the reconstructed low-order flow fields using the first and second pairs of POD modes, which correspond to the Karman-like vortex and its second-order harmonic structure, respectively, are separately defined as

$$v_{\text{rec}12}(x, y, t) = a_1(t)\phi_1(x, y) + a_2(t)\phi_2(x, y), \tag{4}$$

$$v_{\text{rec}34}(x, y, t) = a_3(t)\phi_3(x, y) + a_4(t)\phi_4(x, y). \tag{5}$$

These two events are then phase averaged with an average bin of ±5° in reference to the Karman-like vortex shedding process (Fig. 9). Figure 10 plots the coupled behavior of the phase-dependent Karman-like vortex shedding process (Fig. 10a) and its harmonic event (Fig. 10b). As shown in Fig. 10a, a complete process of the alternatively shedding counterclockwise and clockwise large-scale vortical structures is readily observable. In phase T/8 (Fig. 10a), a highly deformed slender counterclockwise vortical structure is immediately recognizable behind the circular cylinder in the region of $x/D < 1.0$, while a clockwise structure is formed above the downstream station $x/D = 1.5$. In phase T/4, the slender structure has become a large round structure, while the downstream clockwise structure is situated outside of the concerned region. Further growth in the streamwise size is observed with the counterclockwise structure in phase 3T/8, along with the increasing strength, which is reflected in the rotating speed. Because this structure has moved away from the cylinder in phase T/2, a highly deformed complex pattern can be observed immediately behind the cylinder ($x/D < 1.0$), which becomes a slender clockwise vortical structure in phase 5T/8. Similar phase-dependent variations in the clockwise vortical structure are found in the subsequent phases (3T/8–T). Because the Karman-like vortex shedding process is used as the phase reference, the phase-
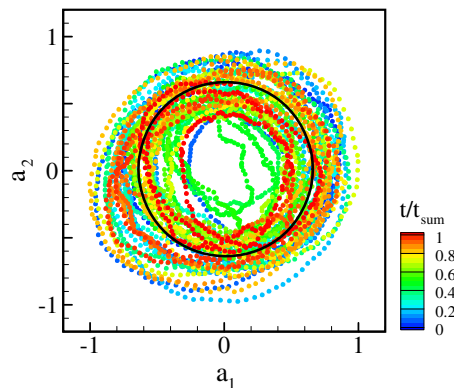

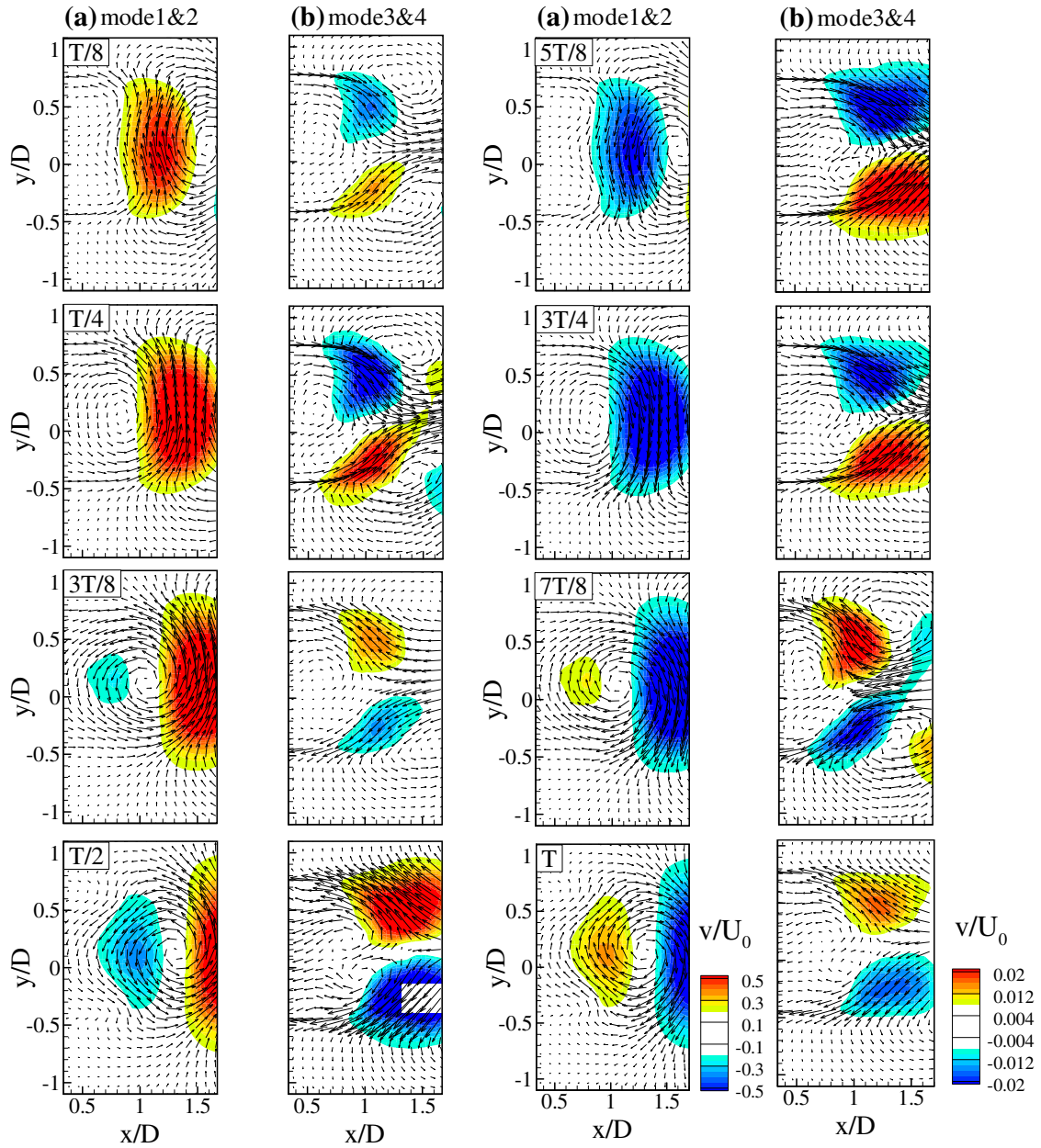**Fig. 9** Correlation map of the first two POD mode coefficients at $\tau = 50$ μs ($U_0 = 5$ m/s)

Fig. 10 Phase-dependent flow fields reconstructed using the first pair (**a**) and the second pair (**b**) of POD modes at $\tau = 50$ μs ($U_0 = 5$ m/s)

dependent variation of the harmonic event shown in Fig. 10b includes two shedding processes in the phases T/8–T. In phase T/8, counterclockwise and clockwise structures are detected at the streamwise station, $x/D = 1.4$, in the upper and lower shear layers, respectively. The strength of the structure becomes intensified at phase T/4, which is reflected in the increasing rotating velocity. However, the full spatial patterns of these structures are readily observed in phases T/8 and T/4. In phase of 3T/8, the rotating direction of the structures is totally reversed, while only a partial extent of the structures can be resolved in the concerned region. In phase T/2, although the structures are not covered in the concern region, the increasing strength is estimated from the considerable increase in the rotating speed. Similar variation of the harmonic event in the other period is observed in phases 5T/8–T. However, no full spatial pattern of the vortical structure of the harmonic event is covered in the limited measurement region in phases 5T/8 and 3T/4. In phase 7T/8, a

clockwise and counterclockwise structure are fully captured at the streamwise station $x/D = 1.5$. These structures are mostly transported out of the region in phase T.

3.2 Wake flow at $U_0 = 10$ m/s

We now examine the TR-PIV measurements at the higher flow speed of $U_0 = 10$ m/s, at which the particle image quality deteriorates due to the reduction in the recognized particle density and the streaky particles that arise from the large exposure time (Fig. 2). Here, a similar comparison is conducted to expose the discrepancies between the TR-PIV measurements with different exposure times and the measurements using the conventional PIV. The time-averaged velocity vector patterns and the streamwise velocity contours are plotted in Fig. 11. The conventional PIV measurements using the pulsed laser show that the recirculation zone has shrunk to $0.7D$ in streamwise direction. However, for the TR-PIV measurements at the shortest exposure time of $\tau = 20$ μs (Fig. 11b), the flow pattern behind the cylinder exhibits considerable discrepancy. Specifically, no recirculation zones are successfully captured immediately behind the cylinder and the "blue" denoted region, which corresponds to the low-speed fluid flow, exhibits rapid contraction until station $x/D = 1.1$, beyond which the region extends downstream, and even expands at $x/D > 1.3$. The high-speed fluid flows denoted in "red" and "yellow" are not accurately represented compared with Fig. 11a. This distinct discrepancy is a result of the highly reduced number of particles that are illuminated at the shortest exposure time. Moving from $\tau = 20$ to 50 μs (Fig. 11c), the recirculation zone can be seen to be successfully determined, and spatial variations of the high-speed and low-speed fluid flows are well represented. Any further increase of the exposure time to $\tau = 80$ μs shows that the streamwise extension of the "blue"-colored low-speed region is overestimated. Of the different exposure times, the TR-PIV measurements using $\tau = 50$ μs show the best performance in capturing the near-wake flow pattern compared with the pattern measured using the conventional PIV.

The profiles of the time-averaged streamwise velocity, the streamwise velocity fluctuation intensity, and the TKE along the various streamwise stations ($x/D = 0.4$–1.2) are plotted in Fig. 12. In contrast to the measurements at $U_0 = 5$ m/s, a distinct discrepancy can be recognized in these profiles with different exposure times when compared with the counterparts determined by the conventional PIV. In the profiles of
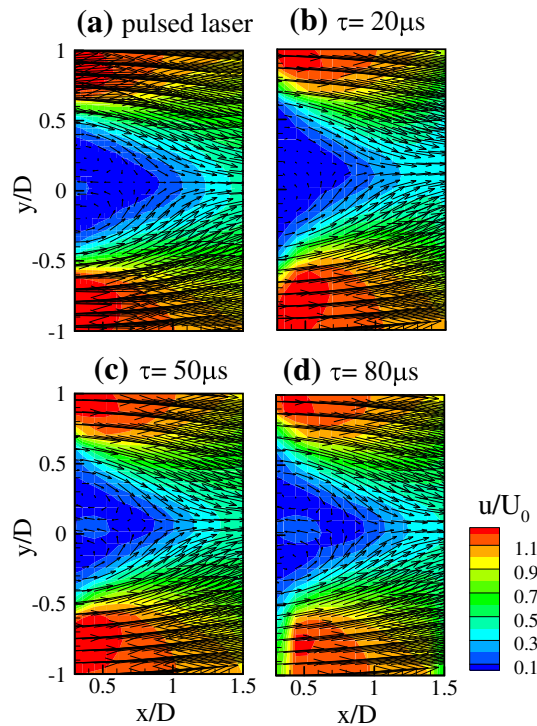

Fig. 11 Vector pattern and contour plot of the time-averaged streamwise velocity ($U_0 = 10$ m/s): pulsed laser (**a**), CW laser with exposure times of 20 μs (**b**), 50 μs (**c**), and 80 μs (**d**)
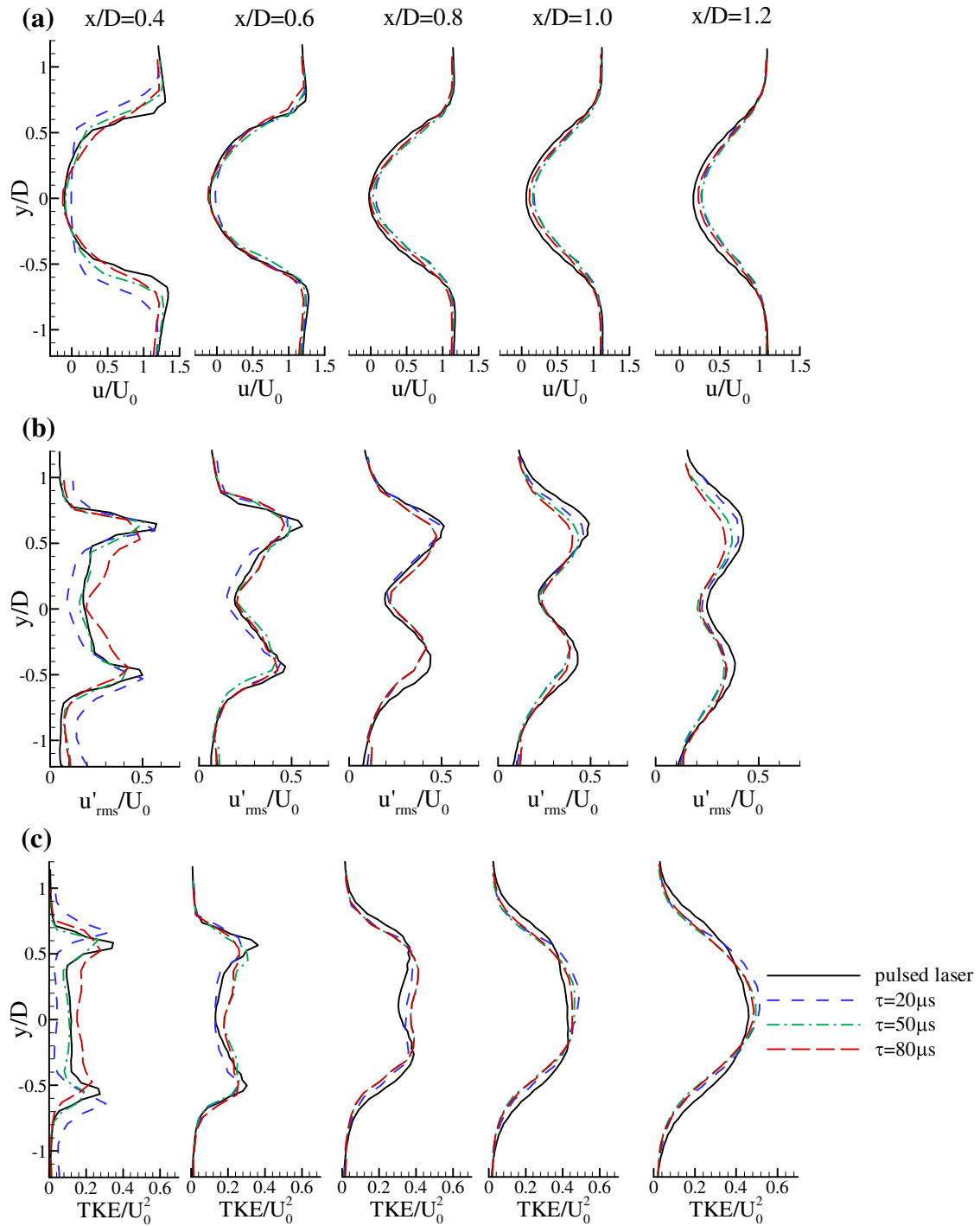
Fig. 12 Profiles of the time-averaged streamwise velocity (**a**), time-averaged streamwise velocity fluctuation intensity (**b**), and turbulence kinetic energy (**c**) along $x/D = 0.4$–1.2 ($U_0 = 10$ m/s)

the time-averaged streamwise velocity shown in Fig. 12a, a prominent discrepancy can be observed in the upper and lower shear layers at station $x/D = 0.4$, especially for the shortest exposure time of $\tau = 20$ μs. The increasing exposure time to $\tau = 50$ μs reduces the discrepancy to a large extent. A further increase to $\tau = 80$ μs results in the flattened variation in the upper and lower separated shear layers, which are dominated by the swirling motion of the underlying vortices, and the fluid flow in the high-speed region is

underestimated. At the subsequent downstream stations until $x/D = 1.2$, the streamwise velocity profiles are much more favorably matched, while the velocity magnitude in the overall reversed flow region is still slightly overestimated in the TR-PIV systems, which can be attributed to the strong swirling motion and the resultant curved image streaking. The velocity calculated in the high-velocity region ($y/D > \pm 0.9$) quantitatively agrees with that in the conventional PIV measurement because the instantaneous fluid flow in this region is more uniform, meaning that the streaking particle image has less influence on the time-averaged velocity in uniform flow region. For the streamwise velocity fluctuation intensity (Fig. 12b), all of the TR-PIV measurements at station $x/D = 0.4$ show a flattened and underestimated peak in the upper and lower shear layers. Moreover, compared with the other two exposure times, the measurement at $\tau = 50$ μs generally matches the conventional PIV measurements, particularly in the bulk recirculation zone. The discrepancy between the TR-PIV measurements progressively increases in the downstream locations, especially around $y/D = \pm 0.5$, which is located on the convecting path of the superimposed large-scale vortical structures, thus indicating that the swirling motion in the local field increases the deviation in the TR-PIV systems. Similarly, as shown in Fig. 12c, the TKE profiles at the nearest station $x/D = 0.4$ exhibit considerable discrepancy. Among the different systems, the measurement at $\tau = 50$ μs favorably agrees with that of the conventional PIV. At the downstream stations, the longitudinal profiles of the TR-PIV measurements show good agreement in terms of the spatial pattern, although the magnitudes are underestimated and overestimated in the separated shear layers and central recirculation zone, respectively. This pattern is closely related to the local flow behavior featured by the swirling vector on the outside, which is revisited in Fig. 15.

The spectral information pertinent to the TR-PIV measurements is identified from the longitudinal velocity spectrum at $x/D = 1$, $y/D = 0.5$, as shown in Fig. 13. An overwhelmingly dominant peak at $St = 0.21$ is detected by all of the systems with the different exposure times, which is assigned to the shedding frequency of the Karman vortex street. Another two peaks can also be discerned at $St = 0.42$ and 0.63 corresponding to the harmonic events. The increasing of exposure time gives rise to a slight reduction in the peak amplitudes because the high-frequency fluctuation is smeared in the long exposure.

We also perform POD analysis of the wake flow at $U_0 = 10$ m/s to examine the spatiotemporal variation in the superimposed flow structures. As shown in Fig. 14, the eigenvalues of the first 10 POD modes show similar trends. For the measurements using the pulsed laser, the energy contributions of the first two modes are 38.5 and 24.2%, respectively, while the contributions of the third and fourth modes are 4.0 and 3.5%, respectively. The energy contribution of the large-scale Karman vortex is relatively higher than that at the low wind speed, which is a result of the stronger intensity of the vortical structures and is consistent with the conclusions drawn on the profiles of the TKE shown in Fig. 12c. For the TR-PIV systems, the eigenvalues of the first two modes are confirmed as 43.0 and 19.8% at $\tau = 20$ μs; 44.4 and 25.0% at $\tau = 50$ μs; and 42.8 and 22.5% at $\tau = 80$ μs, respectively,. Compared to the other energy contributions, the energy contribution
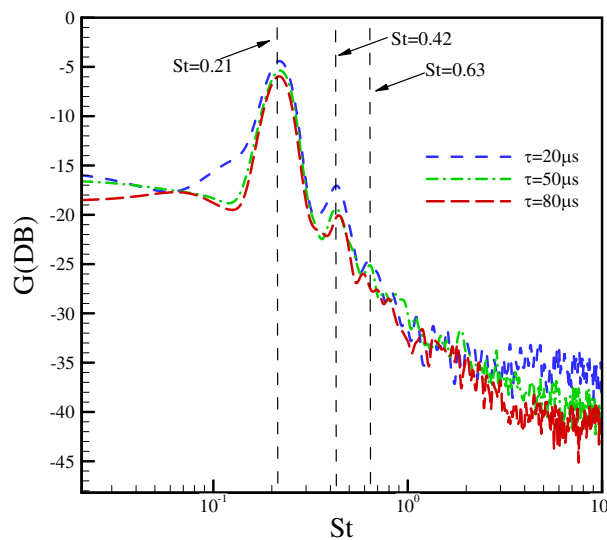

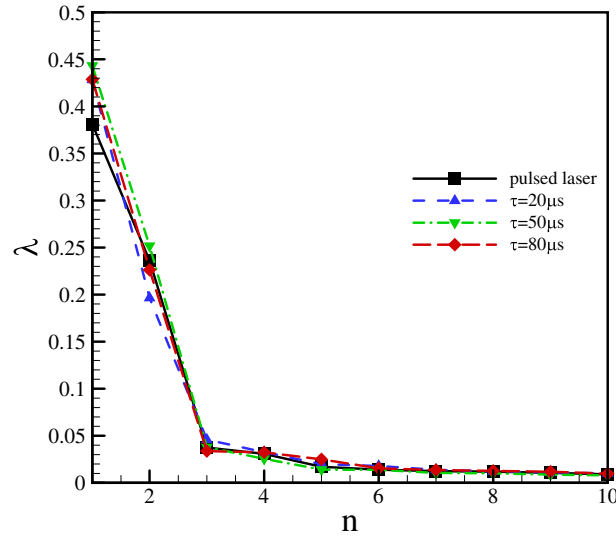**Fig. 13** Streamwise velocity spectra at location ($x/D = 1$, $y/D = 0.5$) ($U_0 = 10$ m/s)

Fig. 14 Eigenvalues of the first ten POD modes of the velocity fields measured with different exposure times ($U_0 = 10$ m/s)

of the second mode in the $\tau = 20$ µs arrangement is quite low, which is due to the failure to identify the recirculation zone (Fig. 11). This issue is revisited as shown in Fig. 15.

The spatial patterns of the first four POD modes are shown in Fig. 15. In the first two POD modes of the conventional PIV (Fig. 15a), a large-scale clockwise vortical structure can be identified at $x/D = 0.8$ in the first mode. In the second mode, a counterclockwise vortical and a clockwise structure are identified at $x/D = 0.4$ and 1.3, respectively. In contrast to the conventional PIV measurements, the TR-PIV measurements using three different exposure times (Fig. 15b–d) show globally similar vector patterns for the first two modes, which reflect the spatial variation of the Karman vortex street. However, in the measurement with exposure time of $\tau = 20$ µs, the clockwise structure in the first mode is underestimated, as shown by the contoured longitudinal component, while the counterclockwise structure in the second mode is not recognized, which explains why the recirculation zone is not identified (Fig. 11). When the exposure time increases to $\tau = 50$ µs, the magnitude of the longitudinal component agrees well with the measurement using the pulsed laser. At the longest exposure time of $\tau = 80$ µs, the vector pattern shows the wrong flow direction in the right corner ($1.4 < x/D < 1.7$, $y/D < -0.5$). For the third and fourth POD modes in the conventional PIV measurement, which correspond to the second-order harmonic structures of the Karman vortex street, a pair of counterclockwise and clockwise vortical structures are identified as closely spaced at station $x/D = 0.5$ in the third mode, while another pair with longitudinal distance $1D$ is found at $x/D = 1.0$ in the fourth mode. For the TR-PIV measurement with $\tau = 20$ µs, no vortical structures are observed in the third mode, although in the fourth mode a pair of vortical structures can be seen at $x/D = 1.0$. As the exposure time increases to $\tau = 50$ and 80 µs, the vortical structures in the third and fourth modes appear in a similar manner, and are generally in conformity with the conventional PIV measurements. However, close comparison shows that the vector pattern in the system with $\tau = 80$ µs deviates distinctly in the region $x/D < 0.6$, $y/D < -0.5$. Inspection of the above four POD modes reveals that there is a strong swirling motion near $y/D = \pm 5$, featured by the anisotropic vector pattern in the Karman vortex street and the harmonic structures, which gives rise to the increased discrepancy in this region (Fig. 12b).

The spectra of the first and third POD mode coefficients for the three TR-PIV systems are plotted in Fig. 16. In the first mode, the peaks are exactly matched at $St = 0.21$ for all three systems with different exposure times. However, the second harmonic event can be discerned in the systems with $\tau = 20$ and 50 µs, and the third harmonic event is evident in all three systems. The occurrence of the high-order harmonic events in the first POD mode coefficient is fundamentally due to the frequency leakage of the POD method (Liu et al. 2014). It is noted that the noise floor in the system with $\tau = 20$ µs is relatively higher than in the other two systems. For the spectra of the third POD mode coefficient, a dominant peak at $St = 0.42$ is detected in all three systems.

We now perform a phase-dependent analysis of the unsteady flow structures in the system with $\tau = 50$ µs, which showed good agreement with the conventional PIV measurements in terms of the
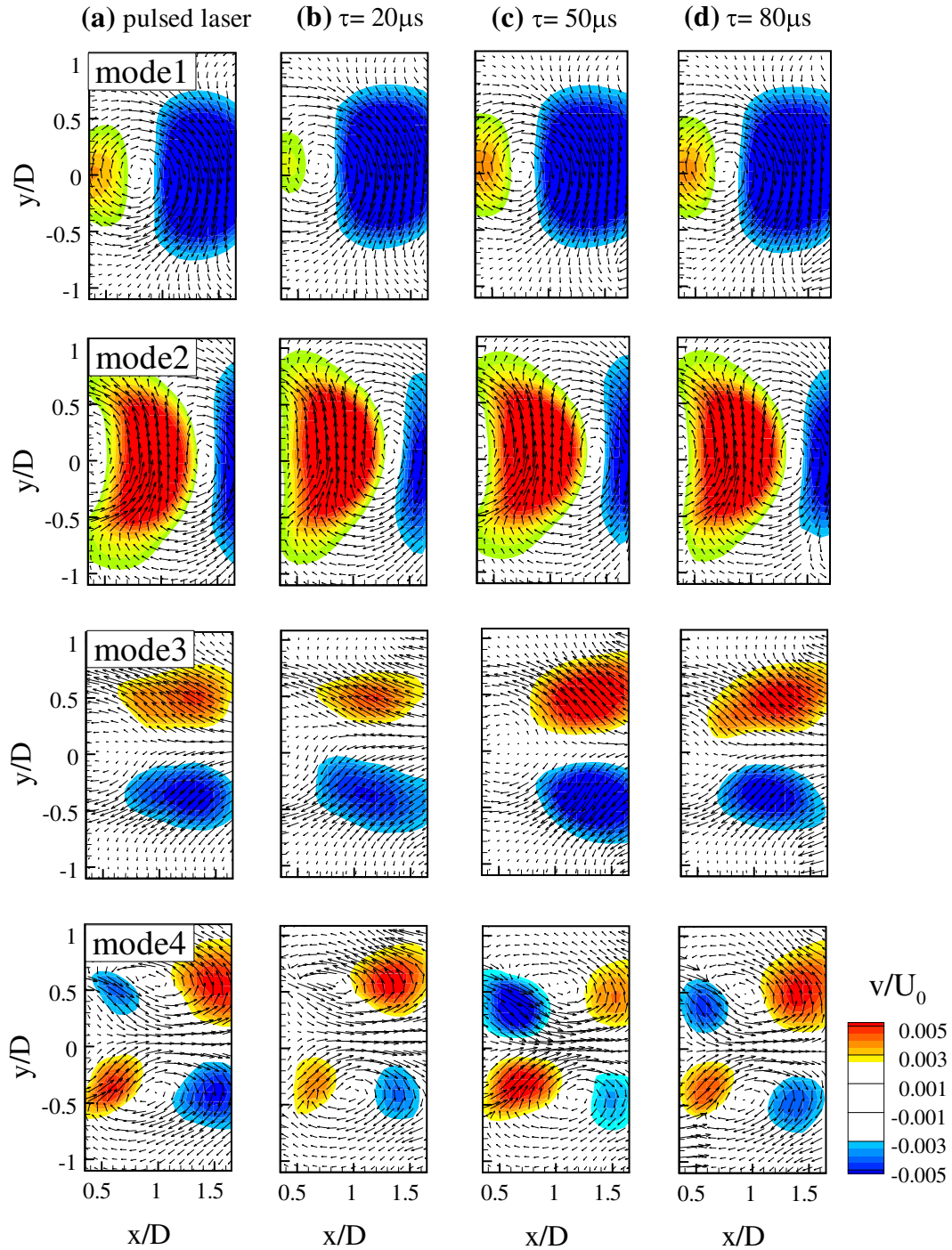
Fig. 15 Spatial patterns of the first four POD modes ($U_0 = 10$ m/s): pulsed laser (**a**), CW laser with exposure times of 20 μs (**b**), 50 μs (**c**), and 80 μs (**d**)

statistical quantities and leading energetic POD modes. As shown in Fig. 17, the correlation between the first two POD mode coefficients is used to determine the cycle-to-cycle variation of the Karman vortex shedding. The shedding processes of the Karman vortex and its second harmonic events are shown in Fig. 18, which are represented by the reconstruction from the first and second pair of POD modes, respectively. In the first half cycle of the period, a counterclockwise Karman vortex forms at $x/D = 0.4$ (T/
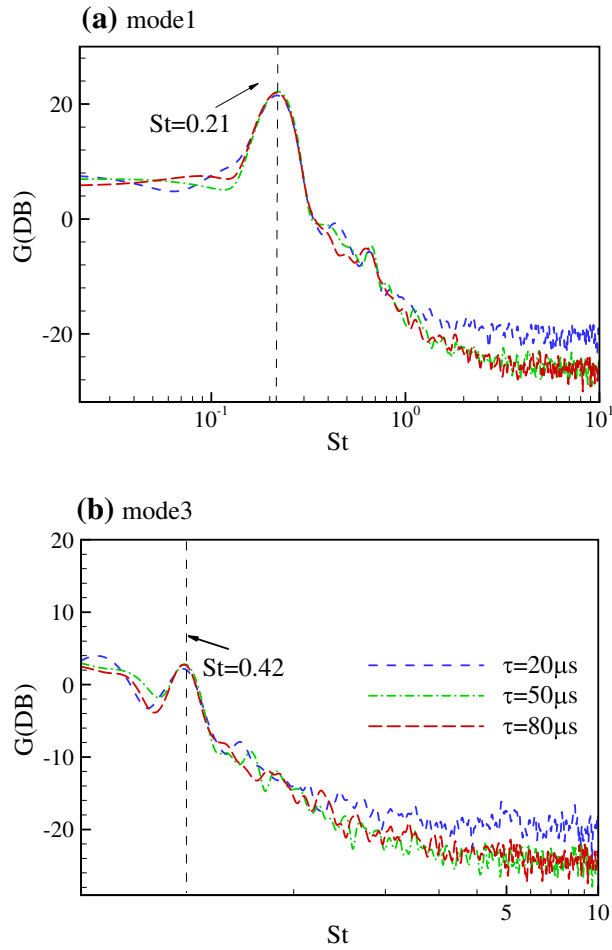
Fig. 16 Spectra of the first and third POD mode coefficients ($U_0 = 10$ m/s)
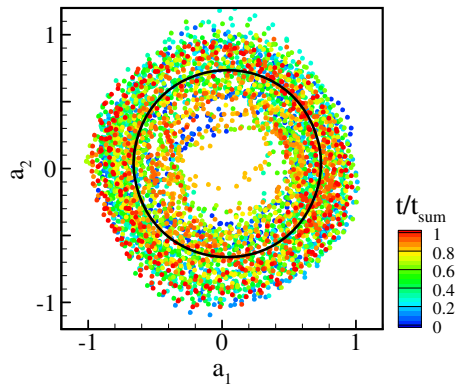

Fig. 17 Correlation map of the first two POD mode coefficients at $\tau = 50$ µs ($U_0 = 10$ m/s)

8) and then continually sheds to the downstream. In the second half cycle of the period, a clockwise Karman vortex forms at the same location and then continually sheds in the downstream direction. In the shedding process of the second-order harmonic events (Fig. 18b), a pair of counterclockwise and clockwise vortical structures are identified in the measured domain around $x/D = 1$, resulting in a total of four localized
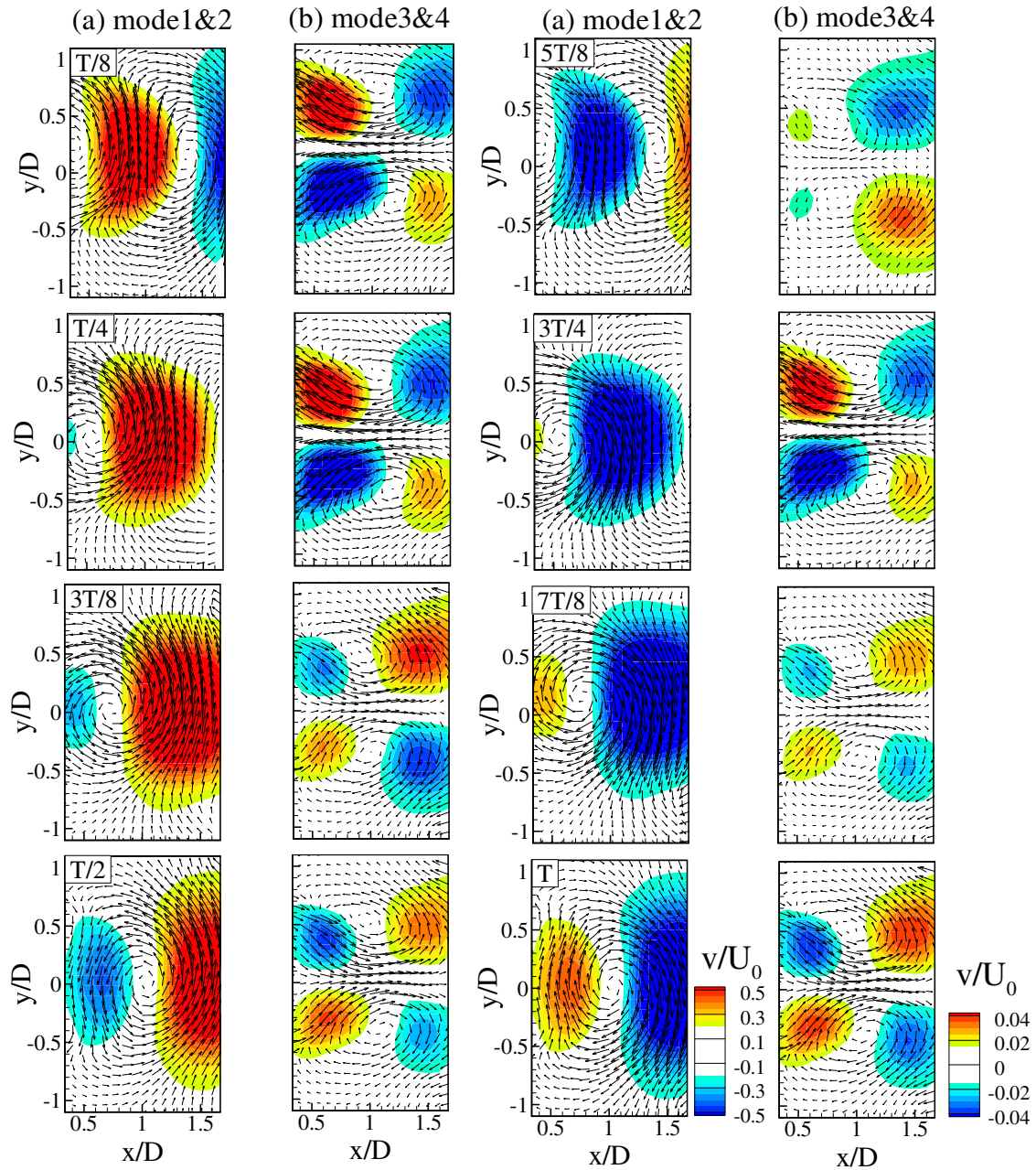
Fig. 18 Phase-dependent flow fields reconstructed using the first pair (**a**) and the second pair of POD modes at $\tau = 50$ μs ($U_0 = 10$ m/s) (**b**)

regions with peak values located around these structures. The rotating direction of the structures is reversed in each period, and two periods are confirmed in one shedding period of the Karman vortex street.

4 Conclusion

In this study, measurement feasibility of unsteady flow structures in the low-speed wind tunnel using the CW laser-based TR-PIV system was extensively evaluated, and the near wake behind a circular cylinder was employed as the benchmark configuration. A CW laser with a maximum power of 25 W combined with a high-speed camera operating at 7 kHz was used to determine the wake flows at two different free-stream

flow speeds: $U_0 = 5$ and 10 m/s. Three different exposure times were selected for the high-speed camera for comparison: $\tau = 20$, 50, and 80 μs. In the experiments, a low-repetition conventional PIV setup using a high-power pulsed laser ($\tau = 8$ ns, 135 mJ/pulse) was used to determine the time-mean and statistical flow quantities, which served as the reference for determining the deviation of the TR-PIV measurements. In the configuration of $U_0 = 5$ m/s, the time-mean-separated flow patterns and streamwise velocity profiles in all of the TR-PIV systems showed satisfactory agreement with the conventional PIV measurements, although a slight discrepancy occurred in high-order quantities such as the streamwise velocity fluctuation intensity and the TKE. In particular, the streamwise fluctuation intensity and the TKE determined by the TR-PIV systems were slightly underestimated and overestimated in the separated shear layers and the recirculation zone, respectively. These deviations increased with the increasing exposure time. Further structural analysis using POD indicated that the large-scale Karman vortex and its harmonic behaviors were well captured by all of the TR-PIV systems. At the higher free-stream flow speed of $U_0 = 10$ m/s, the measurement at $\tau = 50$ μs gave a relatively accurate representation of the time-mean-separated flow pattern, the time-mean streamwise velocity and its fluctuation intensity, and the TKE. The recirculation zone immediately behind the cylinder was not captured in the system with $\tau = 20$ μs, which can be attributed to the inadequate illumination. Considerable deviations in the time-mean streamwise fluctuation intensity and the TKE were observed at station $x/D = 0.4$ when the longest exposure time of $\tau = 80$ μs was used. In the upper and lower separated shear layers with strong unsteady behavior, the streamwise velocity fluctuation intensity was progressively underestimated until $x/D = 1.2$, which can be attributed to the streaky particle image. The strong swirling motion of the convective large-scale vortical structures gave rise to the increased discrepancy near $y/D = \pm 0.5$. Further POD analysis demonstrated that the leading energetic modes in the system with $\tau = 50$ μs accurately determined the spatial features of the Karman-like vortex and its harmonic event. However, the vector representation of the second harmonic events in the system with $\tau = 80$ μs was found to be inaccurate. Finally, for both flow speeds, $U_0 = 5$ and 10 m/s, the lower-order reconstructed phase-dependent variations of the Karman-like vortex and its harmonic behaviors were composed of the time-series velocity vector fields measured in the system with $\tau = 50$ μs, thus providing a straightforward quantitative view of the coupled unsteady events.

It is noted that the measurements using the CW laser-based TR-PIV setup are influenced by various factors like flow speed, laser power, seeding quality, camera sensitivity, its signal-to-noise ratio, and camera exposure time. All of these factors need to be carefully considered in practical situation. In the present study, the TR-PIV measurements obtained on using the state-of-the-art hardware (laser and camera), when the flow speed was less than 10 m/s and the exposure time $\tau = 50$ μs were chosen, agreed well with the flow fields obtained using the conventional PIV setup. Any further increase in the flow speed would not enable accurate representation of the spatiotemporally varying flow structures due to the streaky particle image. However, there is no doubt that the increasing seeding particle's size and the laser power would reduce the optimal exposure time and enlarge the margin of the flow speed.

Compliance with ethical standards

Conflict of interest The authors declare that they have no conflicts of interest in relation to this study.

References

Beresh S, Kearney S, Wagner J, Guildenbecher D, Henfling J, Spillers R, Pruett B, Jiang N, Slipchenko M, Mance J, Roy S (2015) Pulse-burst PIV in a high-speed wind tunnel. Meas Sci Technol 26:095305

Coletti F, Cresci I, Arts T (2013) Spatio-temporal analysis of the turbulent flow in a ribbed channel. Int J Heat Fluid Flow 44:181–196

Elzawawy A (2012) Time resolved particle image velocimetry techniques with continuous wave laser and their application to transient flows[M]. Dissertation, City University of New York

Gurka R, Liberzon A, Hetsroni G (2006) POD of vorticity fields: a method for spatial characterization of coherent structures. Int J Heat Fluid Flow 27(3):416–423

Hout RV (2011) Time-resolved PIV measurements of the interaction of polystyrene beads with near-wall-coherent structures in a turbulent channel flow. Int J Multiph Flow 37:346–357

Kim Y, Rockwell D, Liakopoulos A (2005) Vortex buffeting of aircraft tail: interpretation via proper orthogonal decomposition. AIAA J 43(3):550–559

Liu YZ, Shi LL, Zhang QS (2011) Proper orthogonal decomposition of wall-pressure fluctuations under the constrained wake of a square cylinder. Exp Therm Fluid Sci 35:1325–1333

Liu Y, Zhang Q, Wang S (2014) The identification of coherent structures using proper orthogonal decomposition and dynamic mode decomposition. J Fluids Struct 49:53–72

Sampath R, Chakravarthy SR (2014) Proper orthogonal and dynamic mode decompositions of time-resolved PIV of confined backward-facing step flow. Exp Fluids 55:1–16

Shi LL, Liu YZ, Yu J (2010) PIV measurement of separated flow over a blunt plate with different chord-to-thickness ratios. J Fluids Struct 26:644–657

Shinohara K, Sugii Y, Aota A, Hibara A, Tokeshi M, Kitamori T, Okamoto K (2004) High-speed micro-PIV measurements of transient flow in microfluidic devices. Meas Sci Technol 15(10):1965–1970

Sirovich L (1987) Turbulence and the dynamics of coherent structures. Q J Appl Math 45:561–590

Van Oudheusden BW, Scarano F, Van Hinsberg NP, Watt DW (2005) Phase-resolved characterization of vortex shedding in the near wake of a square-section cylinder at incidence. Exp Fluids 39(1):86–98

Wang S, Liu Y (2016) Wake dynamics behind a seal-vibrissa-shaped cylinder: a comparative study by time-resolved particle velocimetry measurements. Exp Fluids 57:1–20

Wang SF, Liu YZ, Zhang QS (2014) Measurement of flow around a cactus-analogue grooved cylinder at $Re_D = 5.4 \times 10^4$: wall-pressure fluctuations and flow pattern. J Fluids Struct 50:120–136

Willert CE (2015) High-speed particle image velocimetry for the efficient measurement of turbulence statistics. Exp Fluids 56(1):1–17

Zhang QS, Liu YZ (2012) Wall-pressure fluctuations of separated and reattaching flow over blunt plate with chord-to-thickness ratio c/d = 9.0. Exp Therm Fluid Sci 42:125–135